A stochastic view of the 2020 Elazığ Mw6.8 earthquake (Turkey)

Théa Ragon, Mark Simons, Quentin Bletery, Olivier Cavalié, Eric Fielding

A stochastic view of the 2020 Elazığ M_w6.8 earthquake (Turkey)

Théa Ragon[1], Mark Simons[1], Quentin Bletery[2], Olivier Cavalié[2], Eric Fielding[3]

[1]Seismological Laboratory, California Institute of Technology, Pasadena, CA, USA.
[2]Université Côte dAzur, IRD, CNRS, Observatoire de la Côte dAzur, Géoazur, France.
[3]Jet Propulsion Laboratory, California Institute of Technology, Pasadena, CA, USA.

Key Points:

- We infer a stochastic model for the distribution of subsurface fault slip associated with the 2020 Elazığ earthquake
- We account for uncertainties in both the depth-dependence of the assumed elastic structure and the location and geometry of the fault
- Our models are characterized by two primary patches of fault slip where distribution appears to be controlled by geometrical complexities

Corresponding author: Théa Ragon, tragon@caltech.edu

This article has been accepted for publication and undergone full peer review but has not been through the copyediting, typesetting, pagination and proofreading process, which may lead to differences between this version and the Version of Record. Please cite this article as doi: 10.1029/2020GL090704.

Abstract

Until the M_w 6.8 Elazığ earthquake ruptured the central portion of the East Anatolian Fault (EAF, Turkey) on January 24, 2020, the region had only experienced moderate magnitude ($M_w < 6.2$) earthquakes over the last century. We use geodetic data to constrain a model of subsurface fault slip. We adopt an unregularized Bayesian sampling approach relying solely on physically justifiable prior information and account for uncertainties in both the assumed elastic structure and fault geometry. The rupture of the Elazığ earthquake was mostly unilateral, with two primary disconnected regions of slip. This rupture pattern may be controlled by structural complexity. Both the Elazığ and 2010 M_w 6.1 Kovancılar events ruptured portions of the central EAF that are believed to be coupled during interseismic periods, and the Palu segment is the last portion of the EAF showing a large fault slip deficit which has not yet ruptured in the last 145 years.

Plain Language Summary

The Elazığ earthquake ruptured the central portion of the East Anatolian Fault (EAF), a major strike-slip fault in eastern Turkey, on January 24, 2020. Before this event, the region had only experienced moderate magnitude earthquakes over the last century. We aim at understanding the rupture of this earthquake, and how it relates to the historical ruptures of the EAF. To do so, we use measurements of displacement at the surface to image the subsurface slip on the fault that occurred during the earthquake. As the characteristics of the crust are poorly known, we make realistic assumptions on the fault geometry and Earth structure, and build on novel approaches to account for the possible biases of our assumptions and to characterize the uncertainties of the imaged slip. We suggest that the Elazığ earthquake rupture may be controlled by structural complexity of the fault, and that two main regions of slip surround a fault bend acting as a barrier to rupture propagation. We also suggest that the fault segment located between Lake Hazar and the city of Palu is the last portion of the central EAF, showing a large deficit of the fault slip, which has not yet ruptured in the last 145 years.

1 Introduction

A large portion of Turkey is located on the Anatolian Plate (AP), which is slowly extruding westward as a result of the north-south collision between the Arabian and Eurasian tectonic plates (e.g., Mckenzie, 1970; McKenzie, 1972; McClusky et al., 2000). The west-

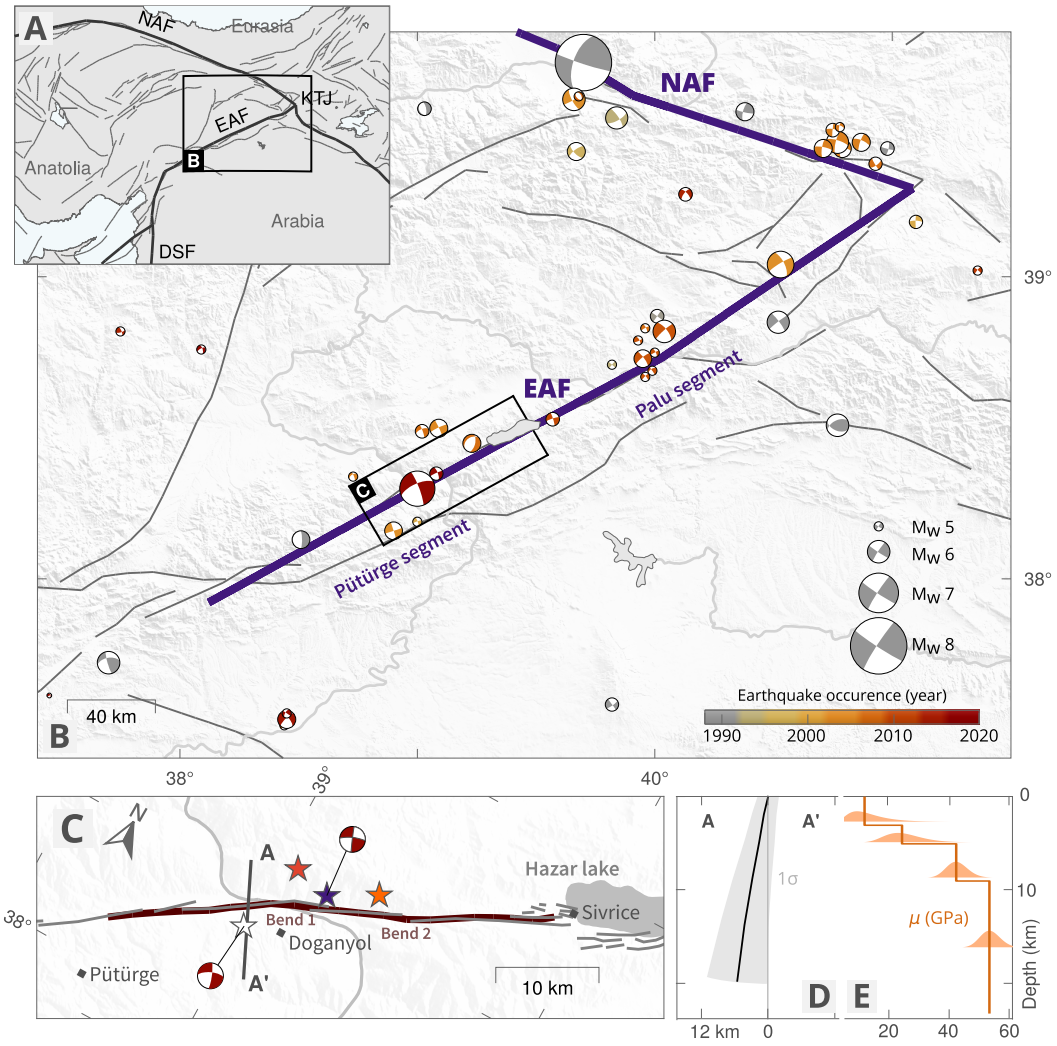

Figure 1. Tectonic setting and assumed characteristics for the Elazığ earthquake. (a) Tectonic setting of the area, plate boundaries are shown in thick black lines. East and North Anatolian Faults are labelled (EAF and NAF), as well as the Dead Sea fault (DSF) and Karlıova Triple Junction (KTJ). (b) Active fault traces (Basilic et al., 2013) and seismicity since 1976 (GCMT, Dziewonski et al., 1981) around the EAF and NAF. The Elazığ earthquake focal mechanism (GCMT) is in red. (c) Details of assumed (dark red) a.nd mapped (gray) fault trace at the surface. Two structural bends of the causative fault geometry are highlighted. Possible epicenters are shown with white, red, purple and orange stars (from left to right on the map), respectively from GCMT, Jamalreyhani et al. (2020), KOERI and AFAD (2020). (d) Assumed fault geometry at depth and associated uncertainty (standard deviation of 5° around the assumed dip and 1 km around the fault surface trace). (e) Assumed shear moduli with depth (derived from Maden, 2012; Ozer et al., 2019) and associated uncertainties.

ward motion of the AP is predominantly accommodated along the North and East Anatolian faults (NAF and EAF, Fig. 1). The NAF experienced a sequence of destructive earthquakes that struck within the last eighty years (e.g., A. Barka, 1996; Stein et al., 1997; Armijo et al., 1999; Şengör et al., 2005). In contrast, the EAF is generally assumed to be less active, and has only experienced small to moderate events over the last century, although large (M > 7) earthquakes have occured in the historical record (e.g., Ambraseys, 1970; Ambraseys & Jackson, 1998; Hubert-Ferrari et al., 2020).

The EAF is a left-lateral 600-km-long strike-slip fault linking the Dead Sea fault (DSF, Fig. 1) to the Karlıova Triple Junction (KTJ, Fig. 1) where it intersects with the right-lateral NAF (e.g., Yilmaz et al., 2006; Duman & Emre, 2013). The EAF has a complex geometry divided into several main segments, each of them characterized by bends, pull-apart basins or compressional structures (e.g., Duman & Emre, 2013), and also comprises multiple secondary sub-parallel and seismically active structures delineating a 50-km-wide fault zone (e.g., Bulut et al., 2012). The EAF accomodates a displacement of 9 to 15 mm/yr (Cetin et al., 2003; Reilinger et al., 2006; Cavalié & Jónsson, 2014; Aktug et al., 2016; Bletery et al., 2020), with creep dominantly at depths greater than 5 km (Cavalié & Jónsson, 2014; Bletery et al., 2020). As a comparison, the NAF shows creep rates around 20-25 mm/yr below a locking depth of 7-25 km (e.g. Cakir et al., 2014a; Hussain et al., 2018; Kaneko et al., 2013; Walters et al., 2011; Wright et al., 2001). Shallower portions of the EAF are characterized by an highly varying inter-seismic slip deficit, some portions being fully coupled while others appear to be at least partially creeping (Bletery et al., 2020).

The January 24 2020 M_w 6.8 earthquake ruptured the EAF between the Hazar Pull-apart Basin and the city of Pütürge (Fig. 1). In the area, the main fault has been mapped, from the interpretation of aerial photos and field studies, as a sinuous trend interrupted by bends and step-overs whose widths do not exceed a kilometer (Duman & Emre, 2013). Coseismic surface rupture does not show a significant horizontal component and is probably mostly gravitational (Tatar et al., 2020). In this study, we investigate the subsurface rupture of the Elazığ earthquake and its relationship to fault geometry and inter-seismic slip deficit. While assuming a fault structure with a realistic geometry, we also account for its inherent uncertainties, as well as uncertainties related to assumptions on the crustal structure. We adopt a Bayesian sampling approach which allows us to sample a large panel of possible slip models and to estimate the posterior uncertainty on the

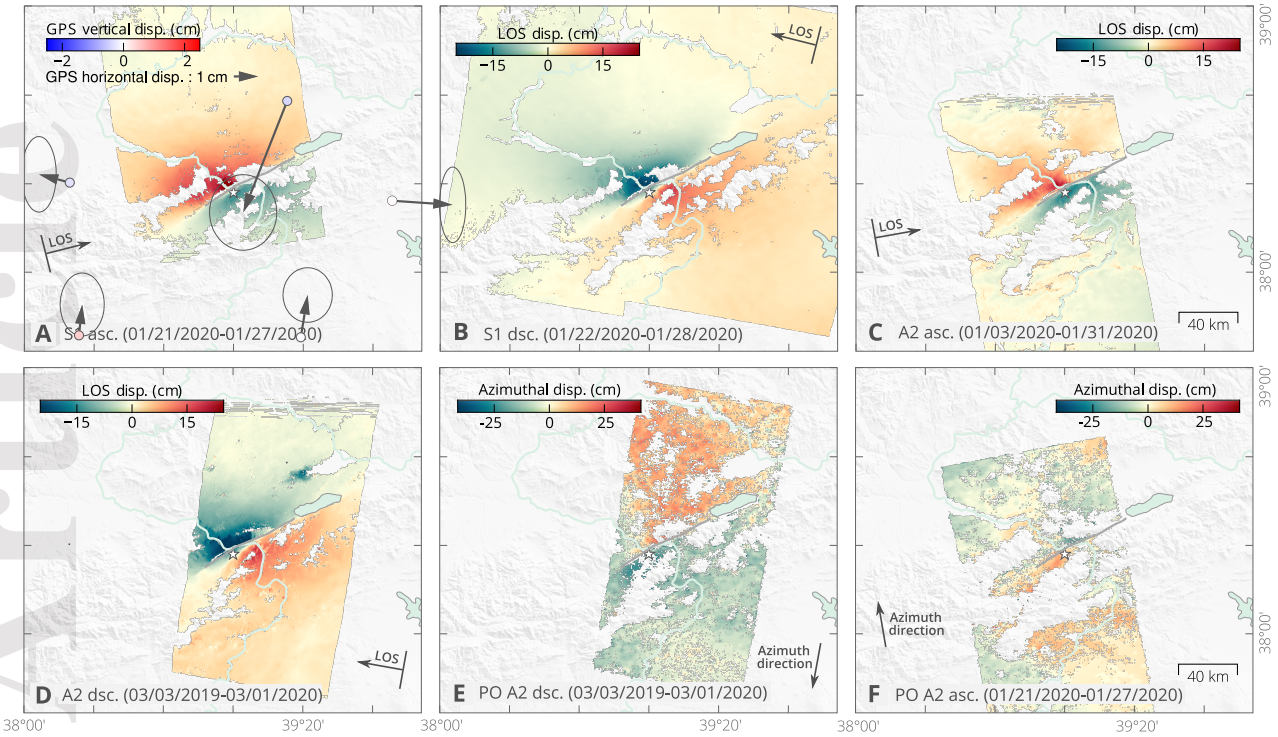

Figure 2. Observations used in thus study. (a) Surface displacement in the satellite line-of-sight (LOS) direction from a Sentinel-1 (S1) ascending (asc.) interferogram, overlayed with coseismic GNSS offsets (Melgar et al., 2020). (b) Surface displacement from a Sentinel-1 descending (dsc.), (c) an ALOS-2 (A2) ascending interferogram, and (d) an ALOS-2 descending interferogram. (e) Pixel-offset (PO) surface displacement in the satellite along-track (azimuth) direction from the ALOS-2 descending pair, and (f) from the ALOS-2 ascending pair. The surface projection of the satellite LOS direction is positive in the ground-to-satellite direction.

inverted slip distribution. This approach allows us to describe the rupture of the Elazığ in detail, while discussing how it may have been driven by structural complexity. Finally, we also provide an updated intepretation of the seismic budget for the central EAF.

2 Bayesian Inference framework

2.1 Data

We derive the earthquake surface displacement from four Synthetic Aperture Radar (SAR) interferometric pairs and two SAR pixel offsets images (summarized in Table S2, Figs 2 and S1 for a closer view on the deformation). We computed two ALOS-2 ascending and descending interferograms, and two Sentinel-1 ascending and descending inter-

ferograms. Copernicus Sentinel-1 data have been acquired by the European Space Agency (ESA) and processed with the NSBAS software (Doin et al., 2012). ALOS-2 data are collected by the Japan Aerospace Exploration Agency (JAXA) and have been processed using the InSAR Scientific Computing Environment (ISCE) software (Rosen, 2012) augmented with an additional module for processing ALOS-2 data (Liang & Fielding, 2017a).

We also applied pixel offset tracking analysis to ALOS-2 images on both tracks (Liang & Fielding, 2017b). Resulting surface displacements have lower precision and higher noise than LOS measurements, but provide useful information on the deformation along the satellite track (azimuthal) direction. Due to snowy conditions in January, both L-band ALOS-2 and C-band Sentinel-1 data decorrelate at higher topographic elevations. Note that surface displacements derived from the InSAR data contain from 3 to 7 days of postseismic deformation, which might affect our modeling of the coseismic phase (Ragon, Sladen, Bletery, et al., 2019; Twardzik et al., 2019). InSAR and dense pixel offsets from the ALOS-2 descending track cover 1 year of preseismic and 1 month of postseismic deformation, and thus also include long-term deformation. To improve computational efficiency, we resample InSAR observations based on model resolution (Lohman & Simons, 2005) with quadtree regions ranging from 12 km to 1.2-2 km wide. We remove data points that are within 500 m of the fault trace to prevent spatial aliasing. We estimate measurement uncertainties following Jolivet et al. (2012, Fig. S2). We also use 3 components coseismic GNSS offsets at 6 stations located within 120 km of the rupture (Fig. 2). These offsets have been processed by Melgar et al. (2020) and extracted from high-rate GNSS displacements.

2.2 Fault geometry and elastic structure

Duman and Emre (2013) mapped the main surface trace of the Pütürge segment as a relatively continuous sinusoidal trend interrupted by small bends and step-overs whose width do not exceed the kilometer. Over the Lake Hazar releasing bend (Fig. 1c), the fault trace divides into multiple parallel lineaments that outline a 10 km wide fault zone (e.g., Garcia Moreno et al., 2011). Around Doğyanol, the fault strike abruptly changes by 10°. West of the rupture area, two major bends affect the Pütürge segment before it links to the Erkenek segment. The strike change around Doğyanol has been well outlined by InSAR data as well (Figs 2, S1), although the rupture did not reach the surface. We build on these observations, as well as on the location of the aftershocks and

previous seismicity (Bulut et al., 2012; Melgar et al., 2020) to define the surface geometry of the causative fault. Hereafter, we will refer to the two bends of the causative fault as the main bend (bend of $\sim 10°$ around the city of Doganyol, refer to Fig. 1c) and the second bend (east of the main bend).

InSAR data show largest amplitudes north of the fault (Fig. 2), suggesting that the fault is slightly dipping northward, as confirmed by the aftershocks (Melgar et al., 2020; Pousse-Beltran et al., 2020). We thus assume a fault dipping of 79° northward (Fig. 1d), from its south-western end to 30 km eastward, the dip angle linearly decreases to 75° further east. We discretize the fault into 203 triangular subfaults whose side range from 1.5 km at the surface to 4-5 km at depth. We also assume a layered crustal model (Tab. S1) derived from the seismic velocity models for NE Turkey proposed by Maden (2012) and by the Vp/Vs ratio proposed by Ozer et al. (2019), and compute coseismic Green's functions following Zhu and Rivera (2002).

2.3 Bayesian Sampling of the inverse problem

In this study, we explore the full solution space of co-seismic slip distributions compatible with geodetic observations in order to sample the range of plausible models. The sampling is performed with a Bayesian approach implemented in the AlTar2 package, originally formulated by Minson et al. (2013). AlTar combines the Metropolis algorithm with a tempering process to iteratively sample the solution space. A large number of samples are tested in parallel at each transitional step, which is followed by a resampling step, allowing us to select only the most probable models. The probability of each sample to be selected depends on its ability to fit the observations $\mathbf{d}_{\text{obs}}$ within the uncertainties $\mathbf{C}_\chi = \mathbf{C}_\text{d} + \mathbf{C}_\text{p}$, where $\mathbf{C}_\text{d}$ represents the observational errors and $\mathbf{C}_\text{p}$ the epistemic uncertainties introduced by approximations of the forward model (e.g., Minson et al., 2013; Duputel et al., 2014; Ragon et al., 2018; Ragon, Sladen, & Simons, 2019).

The solution space is evaluated through repeated updates of the probability density function (PDF) of each sampled parameter

$$p(\mathbf{m}, \beta_i) \propto p(\mathbf{m}) \cdot \exp[-\beta_i \cdot \chi(\mathbf{m})], \tag{1}$$

where $\mathbf{m}$ is the sampled model, $p(\mathbf{m})$ the prior information on this sample, i corresponds to each iteration and β evolves dynamically from 0 to 1 to optimize the parameter space exploration (Minson et al., 2013). $\chi(\mathbf{m})$ is the misfit function which quantifies the dis-

crepancies between observations and predictions within uncertainties described by the covariance matrix $\mathbf{C}_\chi$ (Tarantola, 2005; Minson et al., 2013, 2014; Duputel et al., 2014)

$$\chi(\mathbf{m}) = \frac{1}{2}[\mathbf{d}_{\text{obs}} - \mathbf{G}(\mathbf{m})]^T \cdot \mathbf{C}_\chi^{-1} \cdot [\mathbf{d}_{\text{obs}} - \mathbf{G}(\mathbf{m})]. \quad (2)$$

We solve for both slip amplitude and rake, within the assumed unrestrictive positive uniform prior distribution $p(\mathbf{m}) = \mathcal{U}(0\text{ m}, 20\text{ m})$ for the strike-slip parameters, and within the restrictive Gaussian prior distribution centered on zero for the dip-slip parameters $p(\mathbf{m}) = \mathcal{N}(0\text{ m}, 1\text{ m})$.

Ad-hoc choices of regularization, such as smoothing or moment minimization, artificially restrict the range of possible models and strongly bias the inferred slip distributions towards simplistic overly-smoothed solutions (e.g., Du et al., 1992; Causse et al., 2010). In our approach, we do not impose any type of prior regularization and explore the entire solution space, i.e. the entire range of possible slip models. The final output thus consists in a series of models sampled from among the most plausible models of the full solution space. To explore the results, we consider probabilistic variables, such as a combination of the mean of the sampled models and the associated posterior uncertainty (standard deviation).

2.4 Accounting for epistemic uncertainties

Our estimates of fault slip are driven by the quality and quantity of observations, but also by the way we build the forward model and any other prior information we include in the problem. Any prior choice made to evaluate the Green's function (including problem parameterization and description of the Earth interior) will have a significant impact on inferred model parameters (e.g., Beresnev, 2003; Hartzell et al., 2007; Yagi & Fukahata, 2008; Razafindrakoto & Mai, 2014; Duputel et al., 2014; Gallovič et al., 2015; Diao et al., 2016; Mai et al., 2016). So-called epistemic uncertainties stem from our imperfect description, or simplification, of the parameters describing the Earth interior, such as crustal properties (e.g., rheology), fault geometry or regional characteristics (e.g., topography, Langer et al., 2020). In contrast, aleatoric uncertainties will derive from random, or unknown, processes. In this study, we account for the epistemic uncertainties caused by our poor knowledge of the fault dip, the fault position, and the elastic layered crustal structure, following the methodologies presented by Duputel et

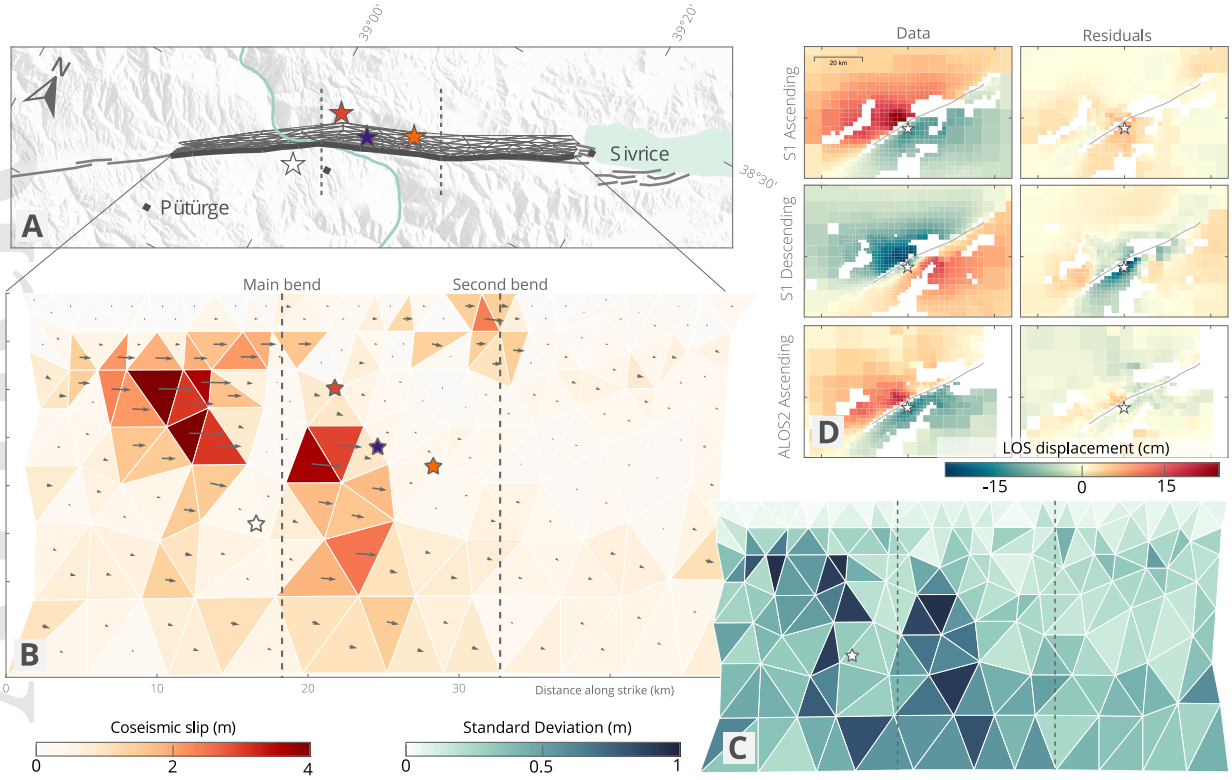

Figure 3. Inferred average slip model and associated posterior uncertainty for the Elazığ earthquake. (a) Map view of the fault trace, subfaults contours at depth and local setting. Possible epicenters are shown with white, red, purple and orange stars (from left to right on the map), respectively from GCMT, Jamalreyhani et al. (2020), KOERI and AFAD (2020). (b) Depth view of the average total slip amplitudes and directions. (c) Standard deviation of the inferred strike-slip parameters. (d) Observed and predicted surface displacement in the LOS direction from Sentinel-1 ascending and descending, and ALOS-2 ascending, InSAR.

al. (2014); Ragon et al. (2018); Ragon, Sladen, and Simons (2019). A part of the aleatoric uncertainties is also quantified with our stochastic approach.

We assume 1 km uncertainty (1σ) in the location of the surface projection of the fault, and 5° uncertainty (1σ) in the fault dip, the fault rotating as a whole around its assumed dip (Fig. 1). We assume uncertainties on the shear modulus for every layer (Poisson's ratio is held constant within each layer), the uncertainty decreasing with depth (Fig. 1, Tab. S1).

3 Results

We infer primarily strike-slip fault slip (Fig. 3). Most of the slip is imaged around the main bend (localized around the city of Doganyol, Fig. 3a). Slip exceeds 3 m within two slip patches, from 2 to 10 km depth west of the main bend and from 7 to 10 km depth east of the main bend. Associated posterior uncertainty for these patches can reach up to ∼1 m for highest amplitudes (Fig. 3c). West of the main bend, the rupture extends down to greater depths (7 - 15 km) with moderate slip amplitudes of ∼2 m. At depth, the posterior model uncertainty reaches up to 1 m. The posterior marginal distributions all show well-delineated Gaussian shapes (Fig. S3), even for the smallest slip amplitudes. The posterior PDFs on subfaults in between these two main slip patches indicate well resolved very low slip amplitudes (Fig. S3), suggesting that the two patches are disconnected (Fig. 3c).

One other narrow slip patch can be observed west of the main bend, at the location of the second bend. Slip is imaged from the surface to 4-km-depth, with maximum amplitudes reaching 2.5 m at the surface, and with relatively small posterior uncertainty. This patch is not connected with the main slip patches, and does not seem to correspond to any $M_w > 4$ aftershock (relocated by Melgar et al., 2020; Pousse-Beltran et al., 2020). This slip may be coseismic or afterslip (given that the InSAR data span a period up to one month after the mainshock).

Observations are well fit by the predictions of our model (Table S3, Figs. 3(d), S5, S6, S7 and S8 for the InSAR and GNSS data respectively), within the assumed uncertainties and possible remaining noise (in particular for the pixel-offset data). Accounting for epistemic uncertainties mitigates overfitting (Ragon et al., 2018). Residuals are expected to be larger than if epistemic biases are neglected. The descending interferograms present larger residuals (Figs. S5, S6, S7) because the assumed fault geometry is primarily constrained by ascending data, and the descending imaging geometry is less favorably oriented (the LOS has a 45° angle with the fault strike).

We also infer the slip distribution of the Elazığ earthquake assuming a planar fault structure dipping of 85° towards the north and embedded within a homogeneous half space, without introducing any epistemic uncertainty (Fig S9). Unlike our preferred model, the slip is concentrated in a single shallow and extended slip patch with low posterior uncertainty. Highest amplitudes (up to 3.5 m) are reached above the main bend, from

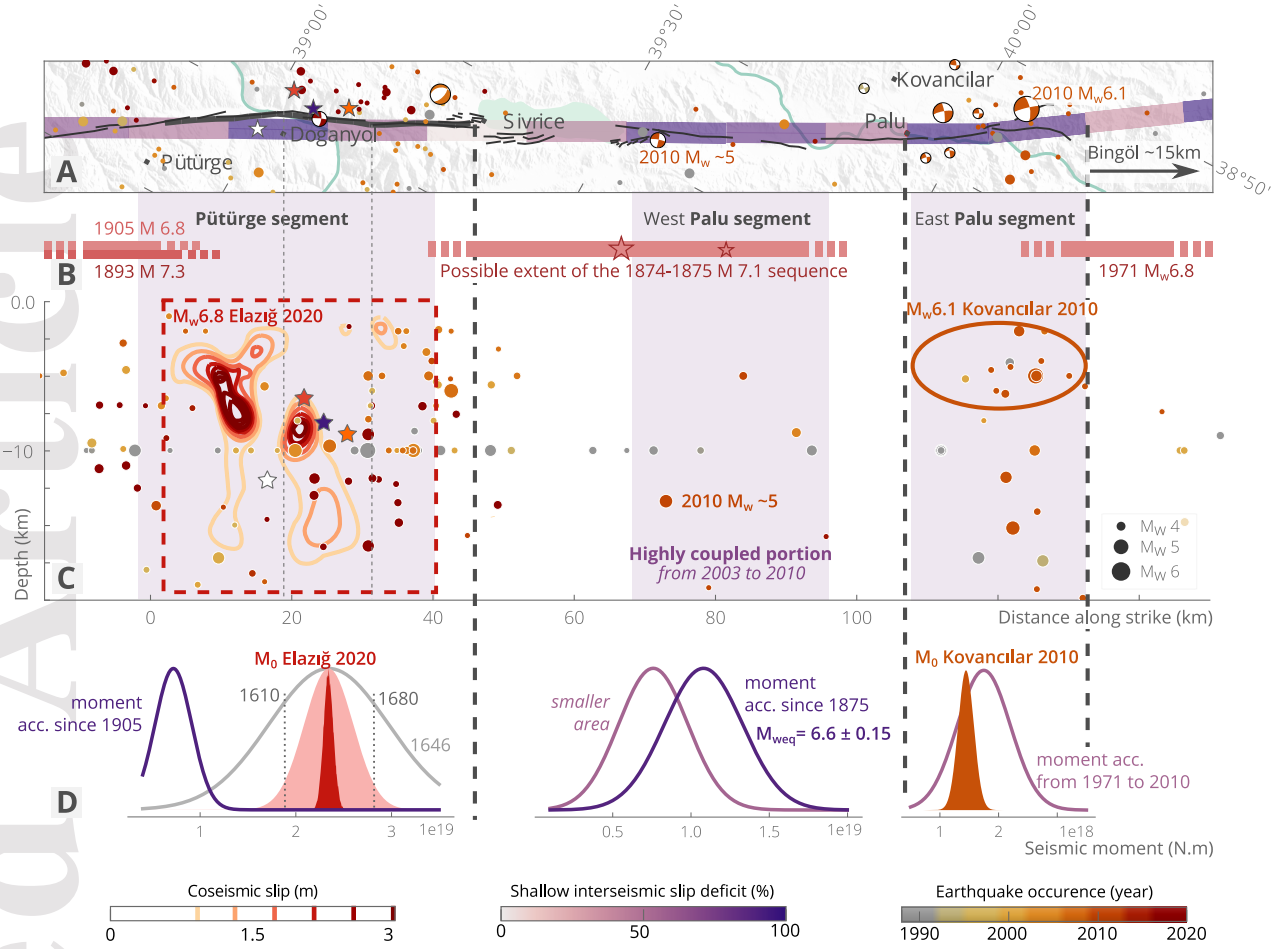

Figure 4. Comparison between the spatial distributions of the 2020 Elazığ earthquake rupture, historical earthquakes, highly coupled sections of the EAF, and seismic moment accumulated since last historical rupture in relation with seismic moment released by the most recent event. (continued)

1.5 to 9 km depth. Low slip values are inferred at depths greater than 10 km and lower than 1.5 km. Some slip is also inferred around the second bend. As expected, the fit of the predicted displacement to the observations is good (Table S3, Figs. S10, S11, S12 and S13), descending interferograms still presenting larger residuals, and slightly better than with our preferred inference.

4 Discussion and Conclusion

Figure 4. Comparison between the spatial distributions of the 2020 Elazığ earthquake rupture, historical earthquakes, highly coupled sections of the EAF, and seismic moment accumulated since last historical rupture in relation with seismic moment released by the most recent event. (A) Map view of two segments the East Anatolian Fault (black lines), overlayed with historical and recent seismicity from 1900 to January 2020 (Retrieved from AFAD, 2020; NEIC, 2020; Melgar et al., 2020), shallow interseismic slip deficit (Bletery et al., 2020) and our assumed fault trace for the 2020 Elazığ event (thick black line). (B) Possible rupture extents for the 4 most recent $M_w > 6.5$ earthquakes that struck the mapped segments of the EAF before the Elazığ event, inferred from Ambraseys (1989); Hubert-Ferrari et al. (2020). Red stars denote the locations of the mainshock and aftershock of the 1874 sequence (Ambraseys, 1989). Fault segments of the central EAF are indicated, from Duman and Emre (2013). (C) Depth extent of the slip amplitude inferred for the 2020 Elazığ event (Fig. 3), along with the highly coupled sections of the EAF between 2003 and 2010 (Bletery et al., 2020), and the possible extent of the 2010 M_w 6.1 Kovancılar earthquake estimated from the spatial coverage of aftershocks and basic scaling laws (Wells & Coppersmith, 1994; Tan et al., 2011), as well as historical and recent seismicity from 1900 to January 2020. (D) For highly coupled portion of each segment, comparison of PDFs of accumulated seismic moment since last historical rupture (in purple), with the seismic moment (M_0) of last recent earthquakes, i.e. the 2020 Elazığ (red) or 2010 Kovancılar (orange) events. For the Pütürge segment, the PDF and mean of accumulated seismic moment since the time needed to accumulate the Elazığ event M_0 are shown in gray, and the PDFs of the Elazığ M_0 are derived from our preferred slip model (red), with a version accounting for uncertainties in the shear modulus ($\mu = 2.8 \pm 0.3\ 10^1$ GPa, light red).

4.1 A stochastic view of the 2020 Elazığ coseismic rupture

Assuming a realistic fault geometry and cristal structure, and accounting for related epistemic uncertainties, we estimate the slip distribution of the 2020 Elazığ earthquake with a Bayesian inference approach. We show that the coseismic rupture affects almost the full width of the Pütürge segment, down to 15-km-depth, with a geodetic moment $M_0 = 2.34 \pm 0.25\ 10^{19}$ N $\cdot$ m and an equivalent moment magnitude of 6.84 ($\mu = 2.8 \pm 0.3\ 10^1$ GPa). Two disconnected slip patches host most of the slip: one patch shows slip exceeding 3 m from $\sim$ 3 to $\sim$ 10 km depth east of the main bend, while the second slip patch extends from 7-km-depth down to 15-km-depth with slip amplitudes larger than 2 m just west of the main bend (Fig. 3).

A large shallow slip (0-5 km, 2.5 m in amplitude) is also imaged around the second bend. While the standard deviation associated with this shallow slip patch is relatively small, its amplitude is poorly constrained by scarce, and possibly noisy, data points largely affected by snowy conditions (Figs. S5, S6, S7). Some of our InSAR data covering up to one month after the mainshock, some imaged deformation, such as this shallow patch, might actually be postseismic. Yet, the surface displacement from 1 week to 5 months after the mainshock does not reach more than a few centimeters (Fig. S14), suggesting that, if afterslip occurred, it was in the hours following the mainshock and with a limited amplitude (as the amplitude of early afterslip often scales with the longer term postseismic deformation, e.g., Twardzik et al., 2019), thus probably not excessively affecting our slip estimates.

The inferred slip distribution changes significantly if we assume a planar fault embedded in a homogeneous crust and we neglect uncertainties stemming from the assumption of a simplified Earth interior. In particular, a single and shallower slip patch is inferred around the epicenter, no slip larger than 50 cm being imaged above 2 km, or larger than 80 cm below 10 km depth. The pronounced slip deficit imaged when assuming a simplified forward model (Fig. S15) might suggest that the shallow slip deficit observed by Pousse-Beltran et al. (2020) may be an artifact deriving from modeling choices, as proposed by Xu et al. (2016) and Ragon et al. (2018).

The location of the epicenter, as estimated from different institutions and authors, comes with more than 16 and 20 kilometers uncertainty in depth and position, respectively (e.g., Jamalreyhani et al., 2020; Tatar et al., 2020). While some models proposed a location around the main bend, many others proposed epicenters rather located in between the two bends (Fig. 3). Robust interpretation on rupture directivity is largely affected by uncertainty in epicenters location, although our results suggest the rupture of the Elazığ earthquake might be mostly unilateral to the SW.

Our estimates of the pattern of fault slip differ from other estimates based on similar data (e.g., Melgar et al., 2020; Pousse-Beltran et al., 2020; Cheloni & Akinci, 2020; Doğru et al., 2020). Our preferred model is very different from Pousse-Beltran et al. (2020); Cheloni and Akinci (2020); Doğru et al. (2020), where peak slip reaches only 2 m over the main bend. In contrast, our preferred model shares many characteristics with the preferred one of Melgar et al. (2020), especially for the peak slip location and the over-

all shape of the ruptured areas, although they image large slip values east of the KOERI epicenter. Melgar et al. (2020) preferred model being primarily driven by high-rate GNSS data and assuming a 1D crustal structure, these shared characteristics suggest that assuming a layered crustal model is necessary to infer robust slip estimates in this region.

4.2 Structurally driven slip on the Pütürge segment

Fault segmentation and bends are thought to act as geometric barriers that can influence, or even drive, rupture initiation, termination and propagation (e.g., G. King & Nabelek, 1985; A. A. Barka & Kadinsky-Cade, 1988; Wesnousky, 2006; Duan & Oglesby, 2005; Aochi et al., 2002; Perrin et al., 2016; Klinger, 2010). Similarly, creeping sections might act as barriers to earthquake propagation (e.g., G. C. P. King, 1986; Chlieh et al., 2008; Perfettini et al., 2010; Kaneko et al., 2010).

The coseismic rupture of the Elazığ earthquake likely started in a relatively planar portion of the fault, in between its two main bends (refer to Fig. 3, Jamalreyhani et al., 2020). Similarly, peak slip amplitudes and most of the slip are located in relatively smooth areas, and surround the main bend where well-resolved low slip values have been imaged. The absence of slip in the main bend is a robust characteristic of our preferred slip model, which has not been imaged in previous studies (e.g., Melgar et al., 2020). The event thus likely ruptured a first portion of the Pütürge segment, stopped at the main bend acting as a barrier, and then broke a second portion, a process that has been observed in numerical simulations (e.g., Kato et al., 1999; Duan & Oglesby, 2005). A perturbation of the rupture propagation by the main bend well correlates with the apparent rupture velocity decrease around the geometrical complexity (imaged by back-projection of waveforms, Pousse-Beltran et al., 2020), and the two distinct peaks of the source time function (automatically determined, Vallée & Douet, 2016).

Slip slowly decreases towards Lake Hazar (Fig. 4). Aftershocks activity also declines abruptly at the basin boundary (Melgar et al., 2020; Jamalreyhani et al., 2020). The pull-apart basin hosting Lake Hazar might thus have acted as a geometrical barrier to the ruptured asperity (as also observed for the Haiyuan fault, China, Liu-Zeng et al., 2007; Jolivet et al., 2013). To the west, no specific geometrical complexity is imaged at the sur-

face, and the rupture may have stopped at the maximum length of the fault segment (Klinger, 2010).

Finally, the location of the main bend also corresponds to the portion of the EAF that shows maximum shallow interseismic slip deficit (>90%, Fig. 4). Inferred slip partly overlays this portion of maximum slip deficit, but the coseismic rupture also extends over moderately coupled regions (30-40%) at greater depths (from 8 to 15-km-depth). The second bend, to the northeast of the main bend (Fig. 3), is also surrounded by large (>2 m) slip amplitudes at shallow depths.

Altogether, these observations suggest that the distribution of subsurface fault slip during the Elazığ earthquake may largely reflect complexities in the fault geometry. Ruptured portions appear to be relatively smooth. In contrast, the main fault bend likely acted as a barrier to rupture propagation, over which no slip has been imaged, similarly to the structure responsible for the pull-apart basin of Lake Hazar. The bend is not prone either to aseismic slip (at least at shallow depths). The deepest imaged slip patch, down to 15-km-depth, confirms that the seismogenic depth is deeper than 10 km for the central EAF (Bulut et al., 2012). Our results do not seem to corroborate the shallow locking depth (full creep below 5 km) inferred by Cavalié and Jónsson (2014). This behavior appears similar to the NAF, where large earthquakes occur on faults also prone to aseismic slip (Cakir et al., 2005, 2014b; Schmittbuhl et al., 2016).

4.3 Seismic potential of the Palu segment

From Pütürge to Bingöl, interseismic slip deficit above 5-km-depth varies along strike, as inferred from geodetic data from 2003 to 2010 (Bletery et al., 2020, Figs 4, S16). Three main sections of large shallow interseismic slip deficit (>70%) are clearly distinct: one on the Pütürge segment, another on the West Palu segment, and a last one east of the city of Palu, on the East Palu segment. Before the Elazığ event, this portion of the EAF was struck by 4 large earthquakes in the last 200 years. Two M $\sim$ 6.8 and M $\sim$ 7.3 occured west of Lake Hazar in 1893 and 1905 (Ambraseys, 1989). In 1874-1875, a sequence of two M $\sim$ 7.1 and M $\sim$ 6.7 likely struck the region between Sivrice and Palu (Ambraseys, 1989; Cetin et al., 2003; Hubert-Ferrari et al., 2017). East of the locality of Palu, the region around the city of Bingöl was affected by a M_w 6.8 in 1971 (Ambraseys, 1989; Ambraseys & Jackson, 1998).

Slip deficit has accumulated on the EAF since these recent historical ruptures, and the newly coupled portions (from 2003 to 2010) are preferably located in between the historically ruptured segments (Bletery et al., 2020). The 2010 M_w 6.1 earthquake that occurred near Kovancılar (Akkar et al., 2011) appears to have filled the possible seismic gap between the 1874 sequence and the 1971 Bingöl event (Fig. 4B). Similarly, the extent of the Elazığ rupture well overlays with a highly coupled portion of the EAF, and it may have filled a possible gap between the 1893/1905 earthquakes and the 1874 sequence (Melgar et al., 2020; Duman & Emre, 2013).

We compare the seismic moment accumulated since the possible last historic rupture of the Pütürge segment (1905) with the seismic moment released during the 2020 Elazığ earthquake (Fig. 4D). To do so, we calculate the seismic moment for the area ruptured by the event according to our slip model, and account for uncertainties in ruptured area ($\sigma = 3$ km^2), shear modulus ($\mu = 2.8 \pm 0.3\ 10^1$ GPa), coupling and slip rates (according to Bletery et al., 2020). The moment released by the 2020 event is largely greater than the one accumulated since 1905 ($2.34 \pm 0.25 >> 0.72 \pm 0.19\ 10^{19}$ N $\cdot$ m). Around 475 years (since 1646) would be necessary to accumulate the moment released by the Elazığ earthquake, assuming constant coupling and slip rates, confirming that the Pütürge segment did probably not rupture during the last historical events, and effectively was a seismic gap. We make the same comparison for the East Palu segment, and show that the moment released by the 2010 M_w 6.1 Kovancılar earthquake well matches the moment accumulated from the 1971 Bingöl event to 2010 ($1.58 \pm 0.2 \approx 2.19 \pm 0.56\ 10^{18}$ N $\cdot$ m, Fig. 4D), suggesting this portion of the EAF actually ruptured during the 1971 event, and that all of the accumulated moment has been released at the time of the Kovancılar earthquake. Since 2010, the seismic moment of the East Palu segment likely accumulated again to reach $4.48 \pm 0.5\ 10^{17}$ N $\cdot$ m, which corresponds to a $M_w \approx 5.73$

Although the portions of the EAF that have been affected by the Elazığ and Kovancılar events show seismic activity in the 20 years preceding these events, the West Palu segment is characterized by relatively low seismic activity (Fig. 4). Together with the low slip deficit at depth (or shallow 5 km locking depth, Cavalié & Jónsson, 2014; Bletery et al., 2020), the lack of seismicity might suggest that the West Palu segment is creeping. However, this segment also shows large interseismic slip deficit in its shallow portion (< 5-km-depth), and at greater depths even larger than for the Pütürge segment (before the 2020 event, Bletery et al., 2020, Fig. S16). Ground shaking maps de-

rived from press reports and testimonies suggest the 1874 sequence likely initiated at depth just west of Lake Hazar (Ambraseys, 1989), near the epicenter of a $M_w \sim 5$ earthquake that occurred in 2010. The West Palu segment is thus capable of producing large earthquakes. Cheloni and Akinci (2020) also suggest that the Elazığ event led to an increase in the Coulomb stress of the Palu segment. Altogether, these observations suggest that the West Palu segment of the central EAF is likely seismogenic. If it were to rupture, the moment accumulated since 1875 on the highly coupled portion is of $7.58 \pm 2.2\ 10^{18}$ N $\cdot$ m (light purple in Fig. 4D), and may reach $1.08 \pm 0.25\ 10^{19}$ N $\cdot$ m if the rupture extends from Lake Hazar to the city of Palu (dark purple in Fig. 4D), which would correspond to a $M_w \sim 6.6 \pm 0.15$ earthquake.

Acknowledgments

The slip model and data are available at `https://doi.org/10.5281/zenodo.4114109`. We thank an anonymous reviewer and Brendan Crowell for thorough reviews. We are very grateful to Diego Melgar and Brendan Crowell who calculated and provided the GNSS offsets for the coseismic deformation, and their relocated aftershocks catalog, which are both available in Melgar et al. (2020). GNSS data were made available from the Turkish National Permanent GNSS/RTK Network (TUSAGA-Aktif/CORS-TR administrated by General Directorate of Land Registry and Cadastre-TKGM and General Directorate of Mapping-HGM, Ankara, Turkey), thanks to Prof. Tuncay Taymaz and Prof. Taylan calan. Initial aftershocks and phase-arrival catalog has been provided by the Disaster and Emergency Management Presidency of Turkey (AFAD, 2020) for the period 24 January 2020 11 February 2020, and historical/background seismicity catalog was provided by BU-KOERI (`http://www.koeri.boun.edu.tr/sismo/2/en/`) for Turkey from 1992 to 2020. This work contains modified Copernicus data from the Sentinel-1A and -1B satellites provided by the European Space Agency (ESA) that are accessible at `earth.esa.int/eogateway/`. Original ALOS-2 data and products are copyright JAXA and provided under JAXA ALOS Research Announcement 6 (RA6) project 3278. The Bayesian simulations were performed with the AlTar2 package (`github.com/lijun99/altar2-documentation`, only accessible via github at publication date). The Classic Slip Inversion (CSI, `github.com/jolivetr/csi`, only accessible via github at publication date) Python library (Jolivet et al., 2014) was used to build inputs for the Bayesian algorithm, in particular to compute Green's functions. The python module PyDistMesh has been used to build the fault

geometry (Persson & Strang, 2004). Figures were generated with the Matplotlib and Seaborn (`doi:10.5281/zenodo.1313201`) Python libraries and with the Generic Mapping Tools library (Wessel et al., 2019). MS was partially supported by the National Aeronautics and Space Administration under Grant No. 80NSSC19K1499. EF was partially supported by the National Aeronautics and Space Administration Earth Surface and Interior focus area under Grant No. 80NM0018D0004. QB work has been supported by the French government, through the UCA JEDI Investments in the Future project managed by the National Research Agency (ANR) ANR-15-IDEX-01, the ANR S5 Grant No. ANR-19-CE31-0003, and the ANR JCJC E-POST Grant No. ANR-14-CE03-002-01JCJC.

References

AFAD. (2020). *AFAD Earthquake catalogue (1900–Feb 2020), Prime Ministry, Disaster and Emergency Management Pres-.* https://deprem.afad.gov.tr/depremkatalogu?lang=en#.

Akkar, S., Aldemir, A., Askan, A., Bakır, S., Canbay, E., Demirel, İ. O., ... Yenier, E. (2011). 8 March 2010 Elazığ-Kovancılar (Turkey) Earthquake: Observations on Ground Motions and Building Damage. *Seismological Research Letters*, *82*(1), 42–58. doi: 10.1785/gssrl.82.1.42

Aktug, B., Ozener, H., Dogru, A., Sabuncu, A., Turgut, B., Halicioglu, K., ... Havazli, E. (2016). Slip rates and seismic potential on the East Anatolian Fault System using an improved GPS velocity field. *Journal of Geodynamics*, *94-95*, 1–12. doi: 10.1016/j.jog.2016.01.001

Ambraseys, N. N. (1970). Some characteristic features of the Anatolian fault zone. *Tectonophysics*, *9*(2), 143–165. doi: 10.1016/0040-1951(70)90014-4

Ambraseys, N. N. (1989). Temporary seismic quiescence: SE Turkey. *Geophysical Journal International*, *96*(2), 311–331. doi: 10.1111/j.1365-246X.1989.tb04453.x

Ambraseys, N. N., & Jackson, J. A. (1998). Faulting associated with historical and recent earthquakes in the Eastern Mediterranean region. *Geophysical Journal International*, *133*(2), 390–406. doi: 10.1046/j.1365-246X.1998.00508.x

Aochi, H., Madariaga, R., & Fukuyama, E. (2002). Effect of normal stress during rupture propagation along nonplanar faults. *Journal of Geophysical Research: Solid Earth*, *107*(B2), ESE 5-1-ESE 5-10. doi: 10.1029/2001JB000500

Armijo, R., Meyer, B., Hubert, A., & Barka, A. (1999). Westward propagation of the North Anatolian fault into the northern Aegean: Timing and kinematics. *Geology*, *27*(3), 267–270. doi: 10.1130/0091-7613(1999)027⟨0267:WPOTNA⟩2.3.CO;2

Barka, A. (1996). Slip distribution along the North Anatolian fault associated with the large earthquakes of the period 1939 to 1967. *Bulletin of the Seismological Society of America*, *86*(5), 1238–1254.

Barka, A. A., & Kadinsky-Cade, K. (1988). Strike-slip fault geometry in Turkey and its influence on earthquake activity. *Tectonics*, *7*(3), 663–684. doi: 10.1029/TC007i003p00663

Basilic, R., Kastelic, V., Demircioglu, M. B., Garcia Moreno, D., Nemser, E. S., Petricca, P., ... Wössner, J. (2013). The European Database of Seismogenic Faults (EDSF) compiled in the framework of the Project SHARE. doi: 10.6092/INGV.IT-SHARE-EDSF

Beresnev, I. A. (2003). Uncertainties in Finite-Fault Slip Inversions: To What Extent to Believe? (A Critical Review). *Bulletin of the Seismological Society of America*, *93*(6), 2445–2458. doi: 10.1785/0120020225

Bletery, Q., Cavalié, O., Nocquet, J.-M., & Ragon, T. (2020). Distribution of Interseismic Coupling Along the North and East Anatolian Faults Inferred From InSAR and GPS Data. *Geophysical Research Letters*, *47*(16), e2020GL087775. doi: 10.1029/2020GL087775

Bulut, F., Bohnhoff, M., Eken, T., Janssen, C., Kılıç, T., & Dresen, G. (2012). The East Anatolian Fault Zone: Seismotectonic setting and spatiotemporal characteristics of seismicity based on precise earthquake locations. *Journal of Geophysical Research: Solid Earth*, *117*(B7). doi: 10.1029/2011JB008966

Cakir, Z., Akoglu, A. M., Belabbes, S., Ergintav, S., & Meghraoui, M. (2005). Creeping along the Ismetpasa section of the North Anatolian fault (Western Turkey): Rate and extent from InSAR. *Earth and Planetary Science Letters*, *238*(1), 225–234. doi: 10.1016/j.epsl.2005.06.044

Cakir, Z., Ergintav, S., Akoğlu, A. M., Çakmak, R., Tatar, O., & Meghraoui, M. (2014a). InSAR velocity field across the North Anatolian Fault (eastern Turkey): Implications for the loading and release of interseismic strain accumulation. *Journal of Geophysical Research: Solid Earth*, *119*(10), 7934–7943. doi:

10.1002/2014JB011360

Cakir, Z., Ergintav, S., Akoğlu, A. M., Çakmak, R., Tatar, O., & Meghraoui, M. (2014b). InSAR velocity field across the North Anatolian Fault (eastern Turkey): Implications for the loading and release of interseismic strain accumulation. *Journal of Geophysical Research: Solid Earth*, *119*(10), 7934–7943. doi: 10.1002/2014JB011360

Causse, M., Cotton, F., & Mai, P. M. (2010). Constraining the roughness degree of slip heterogeneity. *Journal of Geophysical Research: Solid Earth*, *115*(B5). doi: 10.1029/2009JB006747

Cavalié, O., & Jónsson, S. (2014). Block-like plate movements in eastern Anatolia observed by InSAR. *Geophysical Research Letters*, 26–31. doi: 10.1002/2013GL058170@10.1002/(ISSN)1944-8007.GRLeditorhghlts2014

Cetin, H., Güneyli, H., & Mayer, L. (2003). Paleoseismology of the Palu–Lake Hazar segment of the East Anatolian Fault Zone, Turkey. *Tectonophysics*, *374*(3), 163–197. doi: 10.1016/j.tecto.2003.08.003

Cheloni, D., & Akinci, A. (2020). Source modelling and strong ground motion simulations for the January 24, 2020, Mw 6.8 Elazığ earthquake, Turkey. *Geophysical Journal International*. doi: 10.1093/gji/ggaa350

Chlieh, M., Avouac, J. P., Sieh, K., Natawidjaja, D. H., & Galetzka, J. (2008). Heterogeneous coupling of the Sumatran megathrust constrained by geodetic and paleogeodetic measurements. *Journal of Geophysical Research: Solid Earth*, *113*(B5). doi: 10.1029/2007JB004981

Diao, F., Wang, R., Aochi, H., Walter, T. R., Zhang, Y., Zheng, Y., & Xiong, X. (2016). Rapid kinematic finite-fault inversion for an Mw 7+ scenario earthquake in the Marmara Sea: An uncertainty study. *Geophysical Journal International*, *204*(2), 813–824. doi: 10.1093/gji/ggv459

Doğru, A., Bulut, F., Yaltırak, C., & Aktuğ, B. (2020). Slip distribution of the 2020 Elazığ Earthquake (MW 6.75) and its influence on earthquake hazard in the Eastern Anatolia. *Geophysical Journal International*. doi: 10.1093/gji/ggaa471

Doin, M.-P., Lodge, F., Guillaso, S., Jolivet, R., Lasserre, C., Ducret, G., ... Pinel, V. (2012). Presentation Of The Small Baseline NSBAS Processing Chain On A Case Example: The ETNA Deformation Monitoring From 2003 to 2010 Using

ENVISAT Data. , *697*, 98.

Du, Y., Aydin, A., & Segall, P. (1992). Comparison of various inversion techniques as applied to the determination of a geophysical deformation model for the 1983 Borah Peak earthquake. *Bulletin of the Seismological Society of America*, *82*(4), 1840–1866.

Duan, B., & Oglesby, D. D. (2005). Multicycle dynamics of nonplanar strike-slip faults. *Journal of Geophysical Research: Solid Earth*, *110*(B3). doi: 10.1029/2004JB003298

Duman, T. Y., & Emre, Ö. (2013). The East Anatolian Fault: Geometry, segmentation and jog characteristics. *Geological Society, London, Special Publications*, *372*(1), 495–529. doi: 10.1144/SP372.14

Duputel, Z., Agram, P. S., Simons, M., Minson, S. E., & Beck, J. L. (2014). Accounting for prediction uncertainty when inferring subsurface fault slip. *Geophysical Journal International*, *197*(1), 464–482. doi: 10.1093/gji/ggt517

Dziewonski, A. M., Chou, T.-A., & Woodhouse, J. H. (1981). Determination of earthquake source parameters from waveform data for studies of global and regional seismicity. *Journal of Geophysical Research: Solid Earth*, *86*(B4), 2825–2852. doi: 10.1029/JB086iB04p02825

Gallovič, F., Imperatori, W., & Mai, P. M. (2015). Effects of three-dimensional crustal structure and smoothing constraint on earthquake slip inversions: Case study of the Mw6.3 2009 L'Aquila earthquake. *Journal of Geophysical Research: Solid Earth*, *120*(1), 2014JB011650. doi: 10.1002/2014JB011650

Garcia Moreno, D., Hubert, A., Moernaut, J., Fraser, J., Boes, X., Van Daele, M., ... De Batist, M. (2011). Structure and evolution of Lake Hazar pull-apart Basin along the East Anatolian Fault. *Basin Research*, *23*. doi: 10.1111/j.1365-2117.2010.00476.x

Hartzell, S., Liu, P., Mendoza, C., Ji, C., & Larson, K. M. (2007). Stability and Uncertainty of Finite-Fault Slip Inversions: Application to the 2004 Parkfield, California, Earthquake. *Bulletin of the Seismological Society of America*, *97*(6), 1911–1934. doi: 10.1785/0120070080

Hubert-Ferrari, A., Lamair, L., Hage, S., Schmidt, S., Çağatay, M. N., & Avşar, U. (2020). A 3800 yr paleoseismic record (Lake Hazar sediments, eastern Turkey): Implications for the East Anatolian Fault seismic cycle. *Earth and Planetary*

Science Letters, *538*, 116152. doi: 10.1016/j.epsl.2020.116152

Hubert-Ferrari, A., El-Ouahabi, M., Garcia-Moreno, D., Avşar, U., Altınok, S., Schmidt, S., ... Çağatay, M. N. (2017). Earthquake imprints on a lacustrine deltaic system: The Kürk Delta along the East Anatolian Fault (Turkey). *Sedimentology*, *64*(5), 1322–1353. doi: 10.1111/sed.12355

Hussain, E., Wright, T. J., Walters, R. J., Bekaert, D. P. S., Lloyd, R., & Hooper, A. (2018). Constant strain accumulation rate between major earthquakes on the North Anatolian Fault. *Nature Communications*, *9*(1), 1392. doi: 10.1038/s41467-018-03739-2

Jamalreyhani, M., Büyükakpınar, P., Cesca, S., Dahm, T., Sudhaus, H., Rezapour, M., ... Heimann, S. (2020). Seismicity related to the eastern sector of Anatolian escape tectonic: The example of the 24 January 2020 Mw 6.77 Elazığ-Sivrice earthquake. *Solid Earth Discussions*, 1–22. doi: 10.5194/se-2020-55

Jolivet, R., Duputel, Z., Riel, B., Simons, M., Rivera, L., Minson, S. E., ... Fielding, E. J. (2014). The 2013 Mw 7.7 Balochistan Earthquake: Seismic Potential of an Accretionary Wedge. *Bulletin of the Seismological Society of America*, *104*(2), 1020–1030. doi: 10.1785/0120130313

Jolivet, R., Lasserre, C., Doin, M.-P., Guillaso, S., Peltzer, G., Dailu, R., ... Xu, X. (2012). Shallow creep on the Haiyuan Fault (Gansu, China) revealed by SAR Interferometry. *Journal of Geophysical Research: Solid Earth*, *117*(B6), B06401. doi: 10.1029/2011JB008732

Jolivet, R., Lasserre, C., Doin, M. P., Peltzer, G., Avouac, J. P., Sun, J., & Dailu, R. (2013). Spatio-temporal evolution of aseismic slip along the Haiyuan fault, China: Implications for fault frictional properties. *Earth and Planetary Science Letters*, *377-378*, 23–33. doi: 10.1016/j.epsl.2013.07.020

Kaneko, Y., Avouac, J.-P., & Lapusta, N. (2010). Towards inferring earthquake patterns from geodetic observations of interseismic coupling. *Nature Geoscience*, *3*(5), 363–369. doi: 10.1038/ngeo843

Kaneko, Y., Fialko, Y., Sandwell, D. T., Tong, X., & Furuya, M. (2013). Interseismic deformation and creep along the central section of the North Anatolian Fault (Turkey): InSAR observations and implications for rate-and-state friction properties. *Journal of Geophysical Research: Solid Earth*, *118*(1), 316–331. doi: 10.1029/2012JB009661

Kato, N., Satoh, T., Lei, X., Yamamoto, K., & Hirasawa, T. (1999). Effect of fault bend on the rupture propagation process of stick-slip. *Tectonophysics*, *310*(1), 81–99. doi: 10.1016/S0040-1951(99)00149-3

King, G., & Nabelek, J. (1985). Role of Fault Bends in the Initiation and Termination of Earthquake Rupture. *Science*, *228*(4702), 984–987. doi: 10.1126/science.228.4702.984

King, G. C. P. (1986). Speculations on the geometry of the initiation and termination processes of earthquake rupture and its relation to morphology and geological structure. *pure and applied geophysics*, *124*(3), 567–585. doi: 10.1007/BF00877216

Klinger, Y. (2010). Relation between continental strike-slip earthquake segmentation and thickness of the crust. *Journal of Geophysical Research: Solid Earth*, *115*(B7). doi: 10.1029/2009JB006550

Langer, L., Ragon, T., Sladen, A., & Tromp, J. (2020). Impact of topography on earthquake static slip estimates. *Tectonophysics*, 228566. doi: 10.1016/j.tecto.2020.228566

Liang, C., & Fielding, E. J. (2017a). Interferometry With ALOS-2 Full-Aperture ScanSAR Data. *IEEE Transactions on Geoscience and Remote Sensing*, *55*(5), 2739–2750. doi: 10.1109/TGRS.2017.2653190

Liang, C., & Fielding, E. J. (2017b). Measuring Azimuth Deformation With L-Band ALOS-2 ScanSAR Interferometry. *IEEE Transactions on Geoscience and Remote Sensing*, *55*(5), 2725–2738. doi: 10.1109/TGRS.2017.2653186

Liu-Zeng, J., Klinger, Y., Xu, X., Lasserre, C., Chen, G., Chen, W., ... Zhang, B. (2007). Millennial Recurrence of Large Earthquakes on the Haiyuan Fault near Songshan, Gansu Province, China. *Bulletin of the Seismological Society of America*, *97*(1B), 14–34. doi: 10.1785/0120050118

Lohman, R. B., & Simons, M. (2005). Some thoughts on the use of InSAR data to constrain models of surface deformation: Noise structure and data downsampling. *Geochemistry, Geophysics, Geosystems*, *6*(1), Q01007. doi: 10.1029/2004GC000841

Maden, N. (2012). One-Dimensional Thermal Modeling of the Eastern Pontides Orogenic Belt (NE Turkey). *Pure and Applied Geophysics*, *169*(1), 235–248. doi: 10.1007/s00024-011-0296-0

Mai, P. M., Schorlemmer, D., Page, M., Ampuero, J.-P., Asano, K., Causse, M., ... Zielke, O. (2016). The Earthquake-Source Inversion Validation (SIV) Project. *Seismological Research Letters*. doi: 10.1785/0220150231

McClusky, S., Balassanian, S., Barka, A., Demir, C., Ergintav, S., Georgiev, I., ... Veis, G. (2000). Global Positioning System constraints on plate kinematics and dynamics in the eastern Mediterranean and Caucasus. *Journal of Geophysical Research: Solid Earth*, *105*(B3), 5695–5719. doi: 10.1029/1999JB900351

McKenzie, D. (1972). Active Tectonics of the Mediterranean Region. *Geophysical Journal International*, *30*(2), 109–185. doi: 10.1111/j.1365-246X.1972.tb02351.x

Mckenzie, D. P. (1970). Plate Tectonics of the Mediterranean Region. *Nature*, *226*(5242), 239–243. doi: 10.1038/226239a0

Melgar, D., Ganas, A., Taymaz, T., Valkaniotis, S., Crowell, B. W., Kapetanidis, V., ... Öcalan, T. (2020). Rupture kinematics of January 24, 2020 Mw 6.7 Doğanyol-Sivrice, Turkey earthquake on the East Anatolian Fault zone imaged by space geodesy. *Geophysical Journal International*. doi: 10.1093/gji/ggaa345

Minson, S. E., Simons, M., & Beck, J. L. (2013). Bayesian inversion for finite fault earthquake source models I – theory and algorithm. *Geophysical Journal International*, *194*(3), 1701–1726. doi: 10.1093/gji/ggt180

Minson, S. E., Simons, M., Beck, J. L., Ortega, F., Jiang, J., Owen, S. E., ... Sladen, A. (2014). Bayesian inversion for finite fault earthquake source models – II: The 2011 great Tohoku-oki, Japan earthquake. *Geophysical Journal International*, *198*(2), 922–940. doi: 10.1093/gji/ggu170

NEIC. (2020). *NEIC Earthquake catalogue. National Earthquake Information Centre, On-line Bulletin,.* https://earthquake.usgs.gov/earthquakes/search/.

Ozer, C., Ozyazicioglu, M., Gok, E., & Polat, O. (2019). Imaging the Crustal Structure Throughout the East Anatolian Fault Zone, Turkey, by Local Earthquake Tomography. *Pure and Applied Geophysics*, *176*(6), 2235–2261. doi: 10.1007/s00024-018-2076-6

Perfettini, H., Avouac, J.-P., Tavera, H., Kositsky, A., Nocquet, J.-M., Bondoux, F., ... Soler, P. (2010). Seismic and aseismic slip on the Central Peru megathrust. *Nature*, *465*(7294), 78–81.

Perrin, C., Manighetti, I., & Gaudemer, Y. (2016). Off-fault tip splay networks: A genetic and generic property of faults indicative of their long-term propagation. *Comptes Rendus Geoscience*, *348*(1), 52–60. doi: 10.1016/j.crte.2015.05.002

Persson, P.-O., & Strang, G. (2004). A Simple Mesh Generator in MATLAB. *SIAM Review*, *46*(2), 329–345. doi: 10.1137/S0036144503429121

Pousse-Beltran, L., Nissen, E., Bergman, E. A., Cambaz, M. D., Gaudreau, É., Karasözen, E., & Tan, F. (2020). The 2020 Mw 6.8 Elazığ (Turkey) Earthquake Reveals Rupture Behavior of the East Anatolian Fault. *Geophysical Research Letters*, *47*(13), e2020GL088136. doi: 10.1029/2020GL088136

Ragon, T., Sladen, A., Bletery, Q., Vergnolle, M., Cavalié, O., Avallone, A., ... Delouis, B. (2019). Joint Inversion of Coseismic and Early Postseismic Slip to Optimize the Information Content in Geodetic Data: Application to the 2009 Mw6.3 L'Aquila Earthquake, Central Italy. *Journal of Geophysical Research: Solid Earth*, *124*(10), 10522–10543. doi: 10.1029/2018JB017053

Ragon, T., Sladen, A., & Simons, M. (2018). Accounting for uncertain fault geometry in earthquake source inversions – I: Theory and simplified application. *Geophysical Journal International*, *214*(2), 1174–1190. doi: 10.1093/gji/ggy187

Ragon, T., Sladen, A., & Simons, M. (2019). Accounting for uncertain fault geometry in earthquake source inversions – II: Application to the Mw 6.2 Amatrice earthquake, central Italy. *Geophysical Journal International*, *218*(1), 689–707. doi: 10.1093/gji/ggz180

Razafindrakoto, H. N. T., & Mai, P. M. (2014). Uncertainty in Earthquake Source Imaging Due to Variations in Source Time Function and Earth Structure. *Bulletin of the Seismological Society of America*, *104*(2), 855–874. doi: 10.1785/0120130195

Reilinger, R., McClusky, S., Vernant, P., Lawrence, S., Ergintav, S., Cakmak, R., ... Karam, G. (2006). GPS constraints on continental deformation in the Africa-Arabia-Eurasia continental collision zone and implications for the dynamics of plate interactions. *Journal of Geophysical Research: Solid Earth*, *111*(B5). doi: 10.1029/2005JB004051

Rosen, P. A. G. (2012). The InSAR Scientific Computing Environment. In *9th European Conference on Synthetic Aperture Radar*. Nuremberg, Germany.

Schmittbuhl, J., Karabulut, H., Lengliné, O., & Bouchon, M. (2016). Long-lasting seismic repeaters in the Central Basin of the Main Marmara Fault. *Geophysical Research Letters*, *43*(18), 9527–9534. doi: 10.1002/2016GL070505

Şengör, A., Tüysüz, O., İmren, C., Sakınç, M., Eyidoğan, H., Görür, N., ... Rangin, C. (2005). The North Anatolian Fault: A New Look. *Annual Review of Earth and Planetary Sciences*, *33*(1), 37–112. doi: 10.1146/annurev.earth.32.101802.120415

Stein, R. S., Barka, A. A., & Dieterich, J. H. (1997). Progressive failure on the North Anatolian fault since 1939 by earthquake stress triggering. *Geophysical Journal International*, *128*(3), 594–604. doi: 10.1111/j.1365-246X.1997.tb05321.x

Tan, O., Pabuçcu, Z., Tapırdamaz, M. C., İnan, S., Ergintav, S., Eyidoğan, H., ... Kuluöztürk, F. (2011). Aftershock study and seismotectonic implications of the 8 March 2010 Kovancılar (Elazığ, Turkey) earthquake (MW = 6.1). *Geophysical Research Letters*, *38*(11). doi: 10.1029/2011GL047702

Tarantola, A. (2005). *Inverse Problem Theory and Methods for Model Parameter Estimation*. Society for Industrial and Applied Mathematics.

Tatar, O., Sözbilir, H., Koçbulut, F., Bozkurt, E., Aksoy, E., Eski, S., ... Metin, Y. (2020). Surface deformations of 24 January 2020 Sivrice (Elazığ)–Doğanyol (Malatya) earthquake (Mw = 6.8) along the Pütürge segment of the East Anatolian Fault Zone and its comparison with Turkey's 100-year-surface ruptures. *Mediterranean Geoscience Reviews*. doi: 10.1007/s42990-020-00037-2

Twardzik, C., Vergnolle, M., Sladen, A., & Avallone, A. (2019). Unravelling the contribution of early postseismic deformation using sub-daily GNSS positioning —. *Scientific Reports*, *9*(1), 1775. doi: 10.1038/s41598-019-39038-z

Vallée, M., & Douet, V. (2016). A new database of source time functions (STFs) extracted from the SCARDEC method. *Physics of the Earth and Planetary Interiors*, *257*, 149–157. doi: 10.1016/j.pepi.2016.05.012

Walters, R. J., Holley, R. J., Parsons, B., & Wright, T. J. (2011). Interseismic strain accumulation across the North Anatolian Fault from Envisat InSAR measurements. *Geophysical Research Letters*, *38*(5). doi: 10.1029/2010GL046443

Wells, D. L., & Coppersmith, K. J. (1994). New empirical relationships among magnitude, rupture length, rupture width, rupture area, and surface displacement. *Bulletin of the Seismological Society of America*, *84*(4), 974–1002.

Wesnousky, S. G. (2006). Predicting the endpoints of earthquake ruptures. *Nature*, *444*(7117), 358–360. doi: 10.1038/nature05275

Wessel, P., Luis, J. F., Uieda, L., Scharroo, R., Wobbe, F., Smith, W. H. F., & Tian, D. (2019). The Generic Mapping Tools Version 6. *Geochemistry, Geophysics, Geosystems*, *n/a*(n/a). doi: 10.1029/2019GC008515

Wright, T., Parsons, B., & Fielding, E. (2001). Measurement of interseismic strain accumulation across the North Anatolian Fault by satellite radar interferometry. *Geophysical Research Letters*, *28*(10), 2117–2120. doi: 10.1029/2000GL012850

Xu, X., Tong, X., Sandwell, D. T., Milliner, C. W. D., Dolan, J. F., Hollingsworth, J., ... Ayoub, F. (2016). Refining the shallow slip deficit. *Geophysical Journal International*, *204*(3), 1867–1886. doi: 10.1093/gji/ggv563

Yagi, Y., & Fukahata, Y. (2008). Importance of covariance components in inversion analyses of densely sampled observed data: An application to waveform data inversion for seismic source processes. *Geophysical Journal International*, *175*(1), 215–221. doi: 10.1111/j.1365-246X.2008.03884.x

Yilmaz, H., Over, S., & Ozden, S. (2006). Kinematics of the East Anatolian Fault Zone between Turkoglu (Kahramanmaras) and Celikhan (Adiyaman), eastern Turkey. *Earth, Planets and Space*, *58*(11), 1463–1473. doi: 10.1186/BF03352645

Zhu, L., & Rivera, L. A. (2002). A note on the dynamic and static displacements from a point source in multilayered media. *Geophysical Journal International*, *148*(3), 619–627. doi: 10.1046/j.1365-246X.2002.01610.x

Figure 1.

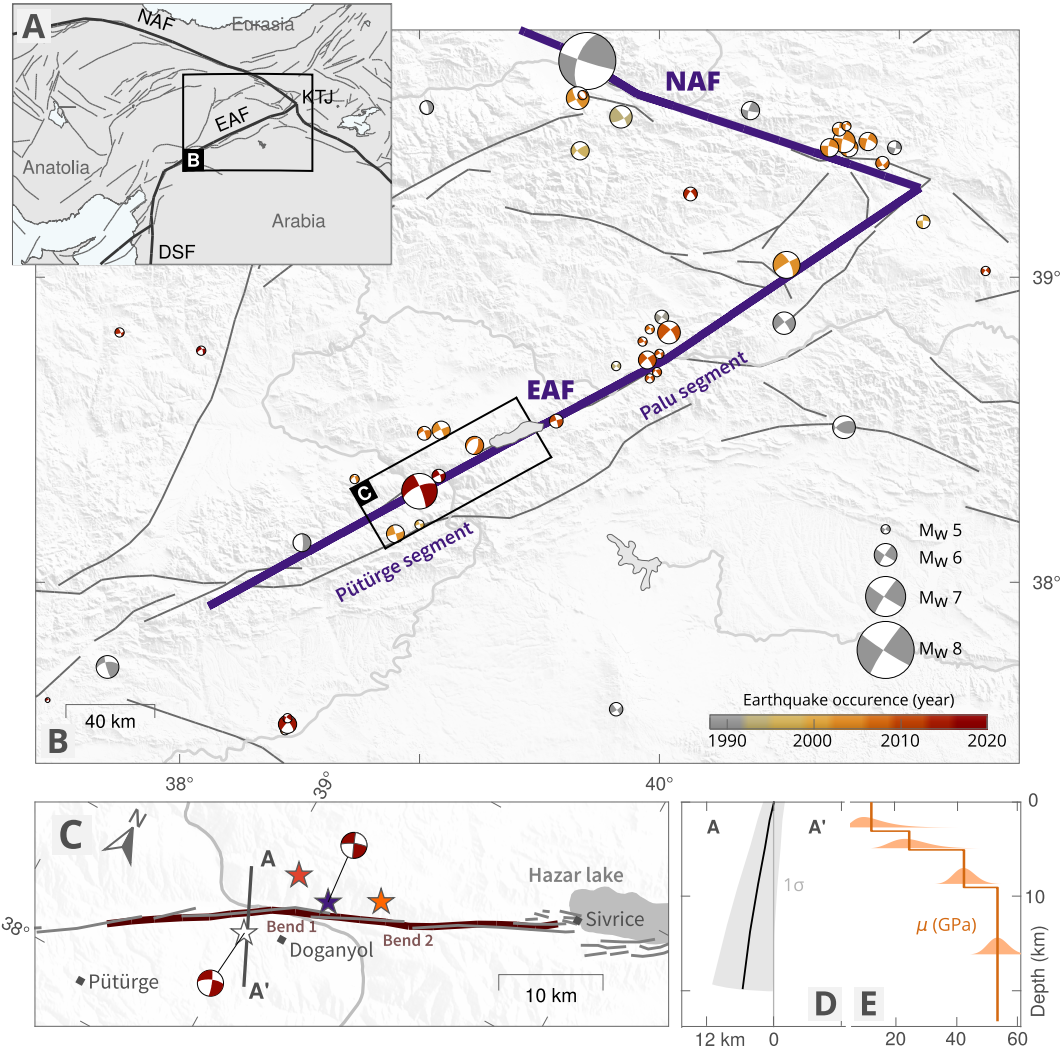
A
NAF
Eurasia
EAF
KTJ
B
Anatolia
Arabia
DSF
NAF
39°
EAF
Palu segment
C
Pütürge segment
38°
Mw 5
Mw 6
Mw 7
Mw 8
Earthquake occurence (year)
1990
2000
2010
2020
40 km
B
38°
39°
40°
C
N
A
Hazar lake
Sivrice
38°
Bend 1
Doganyol
Bend 2
Pütürge
A'
10 km
A
A'
1σ
μ (GPa)
Depth (km)
0
10
D
E
12 km
0
20
40
60

Figure 2.

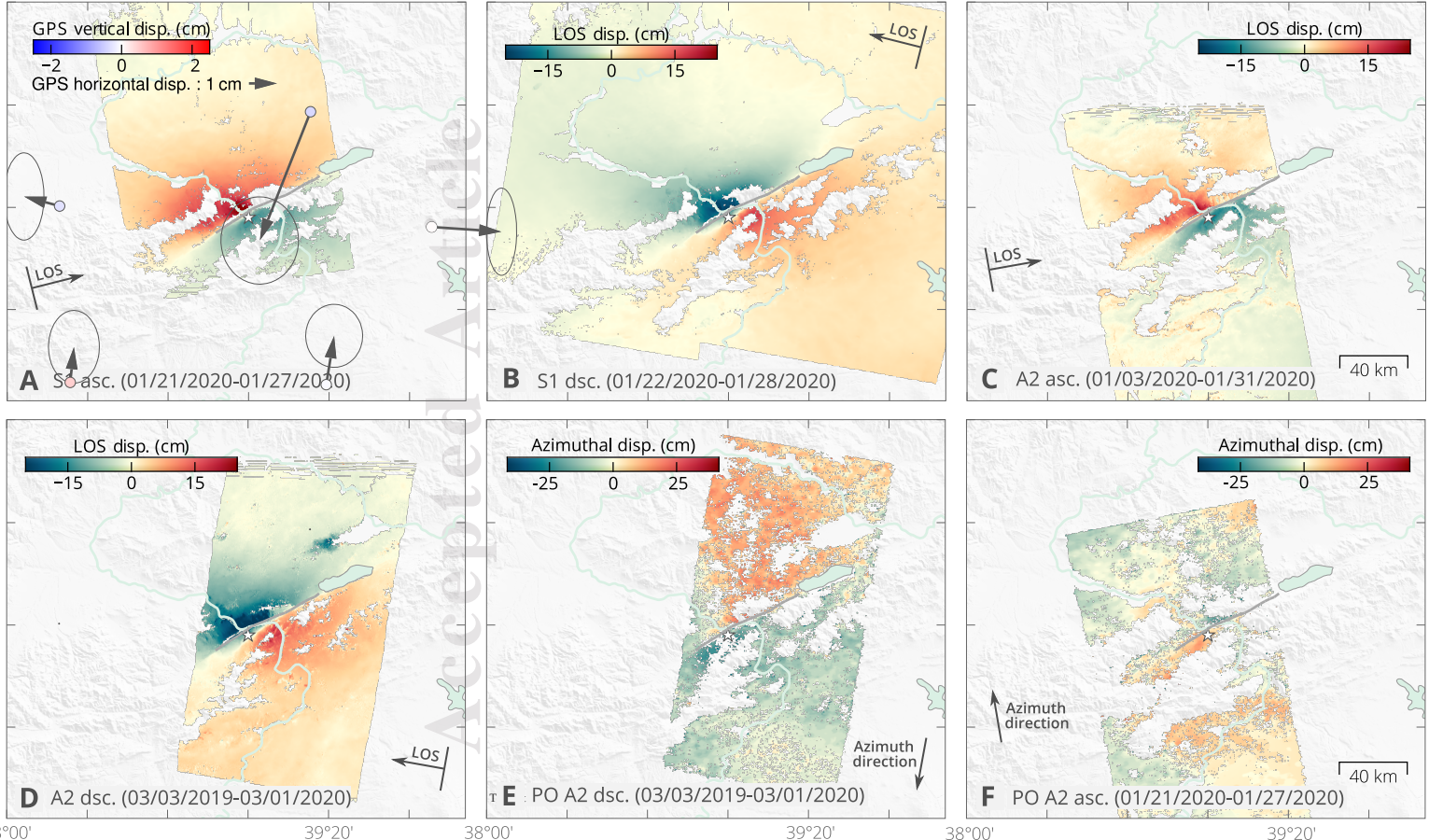

Figure 3.

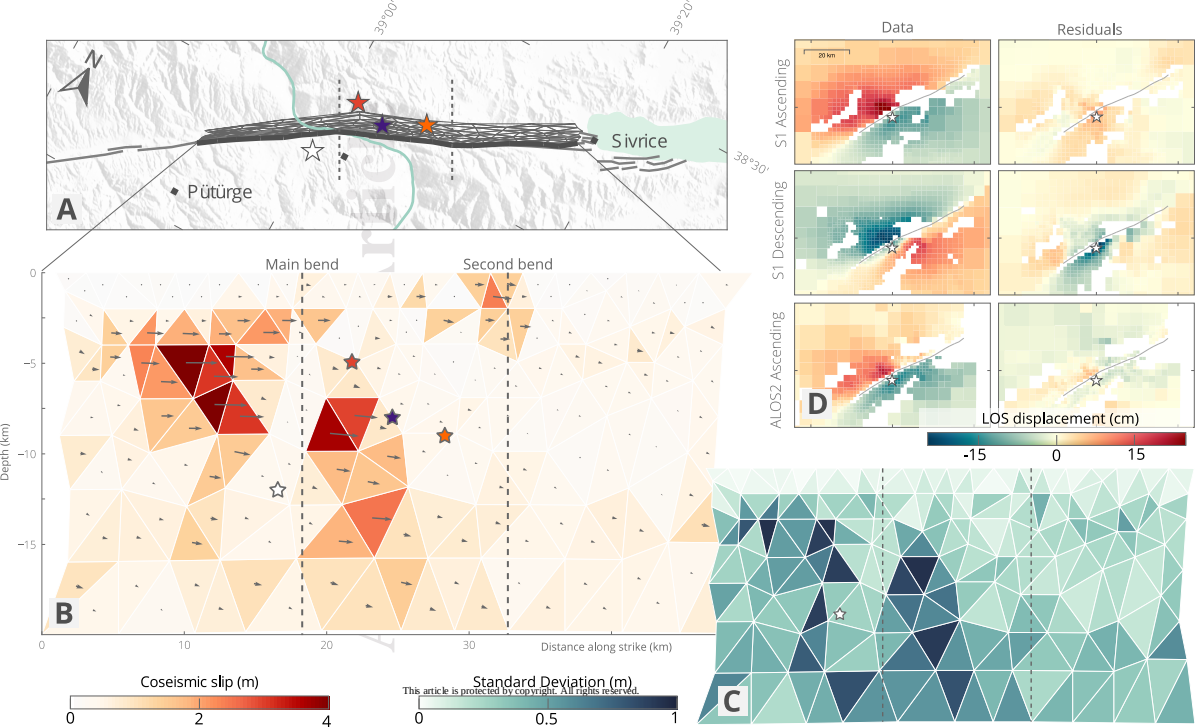

Figure 4.